

## Quantification of Ni-YSZ Anode Microstructure Based on Dual Beam FIB-SEM Technique

H. Iwai<sup>a</sup>, N. Shikazono<sup>b</sup>, T. Matsui<sup>c</sup>, H. Teshima<sup>b</sup>, M. Kishimoto<sup>a</sup>, R. Kishida<sup>c</sup>,  
D. Hayashi<sup>a</sup>, K. Matsuzaki<sup>b</sup>, D. Kanno<sup>b</sup>, M. Saito<sup>a</sup>, H. Muroyama<sup>c</sup>,  
K. Eguchi<sup>c</sup>, N. Kasagi<sup>b</sup>, H. Yoshida<sup>a</sup>

<sup>a</sup> Department of Aeronautics and Astronautics, Kyoto University,  
Sakyo-ku, Kyoto 606-8501, Japan

<sup>b</sup> Department of Mechanical Engineering, The University of Tokyo, Hongo 7-3-1,  
Bunkyo-ku, Tokyo 113-8656, Japan

<sup>c</sup> Department of Energy & Hydrocarbon Chemistry, Kyoto University,  
Nishikyo-ku, Kyoto 615-8510, Japan

Three-dimensional microstructure of a conventional Ni-8YSZ anode is quantified by means of dual beam FIB-SEM system equipped with EDX. The microstructure of the anode is virtually reconstructed in a computational field using a series of two-dimensional SEM images acquired. Three-phase-boundary (TPB) density and tortuosity factors are carefully evaluated applying two different evaluation methods to each parameter. TPB density is evaluated by volume expansion method and centroid method, while tortuosity factor is evaluated by Lattice Boltzmann Method calculation and by random walk approach. The estimations of each parameter by two methods match well each other showing the reliability of analyzing methods proposed in this study.

### Introduction

Solid Oxide Fuel Cell (SOFC) is one of the most promising energy conversion devices due to its high efficiency and fuel flexibility (1). The long-term durability is one of the most important requirements for the practical application of the SOFC system, and great efforts have been paid for developing materials with high stabilities and electrodes with optimal microstructures. Porous Ni-zirconia cermets, e.g. Ni-YSZ, Ni-ScSZ, are the most widely and commonly used anode materials in SOFCs, since they can match the thermal expansion coefficient with that of the electrolyte and can effectively extend reaction sites (three-phase boundary, TPB) with high electrocatalytic activity (2, 3). It is widely recognized that anode microstructure has a significant impact on cell performance as well as cell durability (4-8). For example, effects of morphology change (7-9), dependence on starting materials and fabrication methods have been reported (10-12). However, the quantitative relationship between the anode microstructure and the polarization resistances is not fully understood. Recently, direct measurements of three dimensional SOFC electrode microstructures have been reported using focused ion beam scanning electron microscopy (FIB-SEM) (13-16) and X-ray computed tomography (XCT) (17). Through these three dimensional measurements, important microstructural parameters such as TPB length and tortuosity can be obtained. It is expected that these new methods will serve important information for quantitatively connecting microstructure to polarization characteristics.

In the present study, three dimensional microstructure of the Ni-8YSZ anode is quantified by means of dual beam FIB-SEM. In-lens secondary electron detector was used, which provided clear contrast between Ni and YSZ phases with submicron resolution. From the reconstructed three dimensional structure, microstructural parameters such as volume fraction, TPB length and tortuosity factors are quantified. Different analyzing methods are compared for the acquisition of microstructural parameters.

### **Sample preparation**

The electrode examined in this study is the Ni-YSZ cermet anode (Ni:YSZ=50:50 vol%) of a conventional Ni-YSZ | YSZ | LSM button cell. The anode material, NiO-YSZ, is mixed with poly-ethylene glycol, screen printed on a YSZ electrolyte and sintered at 1400 °C for 5 hours. The cathode of  $(\text{La}_{0.8}\text{Sr}_{0.2})_{0.97}\text{MnO}_3$  (abbreviated as LSM) is also mixed with poly-ethylene glycol to form slurry. It is screen printed on the other face of electrolyte and sintered at 1150 °C for 5 hours. These cells can be applied to the power generation experiments in laboratories. However no power generation test was performed to the sample cells of this study. After reducing the anode at 1000 °C, the cell temperature was decreased to room temperature without experiencing any electrochemical reaction. Samples were infiltrated with epoxy resin (Marumoto struers K. K.) under vacuum condition so that pores of the porous electrode can be easily distinguished during SEM observation. Cured samples were polished by Ar-ion beam cross-section polisher (JEOL Ltd., SM-09010) and supplied for the FIB-SEM observation (Carl Zeiss, NVision 40).

### **FIB-SEM observation**

Observation and quantification of 3-D micro-structure of Ni-YSZ anode are enabled by using FIB-SEM system installed at Kyoto Univ. The FIB-SEM system, NVision 40, is equipped with Gemini FE-SEM column (Carl Zeiss), zeta FIB column (SIINT) and a multi channel gas injection system (SIINT). It also has EDX and EBSD options. Figure 1 schematically shows a typical setting of FIB-SEM observation. In this system, two beams have the coincident angle of 54°. In-lens secondary electron detector was used for the observation in this study with typical acceleration voltage of 1-2kV. A sample electrode is set as shown in the figure. Front part of the target volume is removed by FIB milling prior to the observation. By using the GIS, carbon is deposited on the surface of the target volume to protect it from undesired milling and to prevent charge up of the observation surface. Fig. 2 (a) shows a SEM image of a sample electrode after these preparations. FIB-SEM observation takes following steps. The surface of the observation area is slightly milled by FIB to *z*-direction so that a new *x-y* observation surface is exposed for SEM imaging. By automatically repeating this ion milling and SEM imaging sequence, which is called as “cut-and-see” operation in NVision 40 system, a series of SEM images necessary for 3-D structure analysis is acquired. One more treatment is done in this study before starting the milling and imaging sequence. Image drifting is an unavoidable problem during the image acquisition while precise image alignment is essential for quantitative analysis of the 3-D microstructure. To assist the later alignment process of the SEM images, reference marks are created on the carbon layer deposited on the sample surface using FIB as shown in Fig. 2(b). Sequential data set acquisition by FIB-SEM is conducted at three different locations of a sample anode electrode. Their sizes and spatial resolutions are summarized in Table 1.

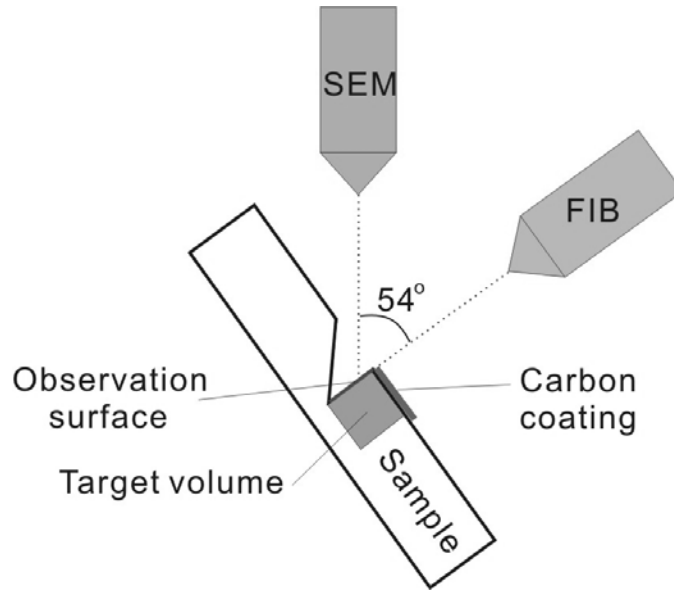


Figure 1. Schematic diagram of FIB-SEM setting.

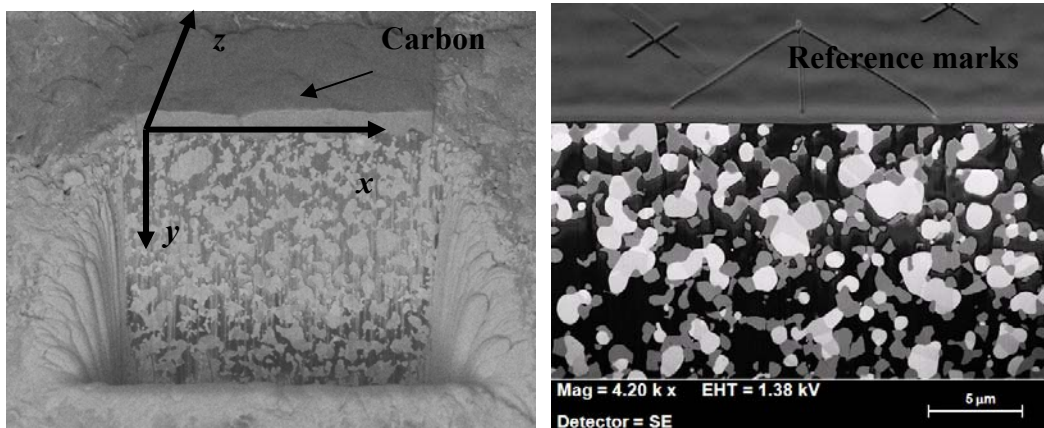


Figure 2. (a) SEM image of a sample anode before “cut-and-see” operation sequence (Left), (b) right: Reference marks created on the carbon coating (Right).

**TABLE I.** Sizes and spatial resolutions of three samples.

		<i>x</i>	<i>y</i>	<i>z</i>
Sample 1	Sample dimension (μm)	26.095	10.906	4.74
	Number of voxels	981	410	79
Sample 2	Sample dimension (μm)	25.722	11.624	6.572
	Number of voxels	967	437	106
Sample 3	Sample dimension (μm)	26.341	10.768	6.048
	Number of voxels	994	407	84

### 3-D microstructure reconstruction

3-D microstructure of Ni-YSZ anode electrode is virtually reconstructed in a computational field using 2-D SEM images obtained through the FIB-SEM observation. The SEM images are firstly aligned based on the reference marks created on the carbon layer deposited on the sample surface as explained in the previous section. It was found

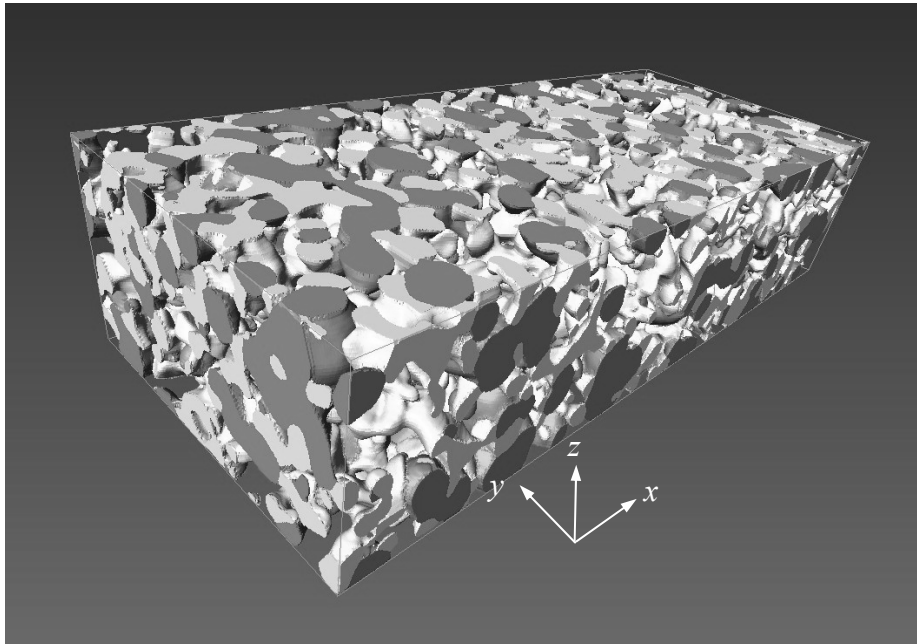


Figure 3. Reconstructed Ni-YSZ anode microstructure (25.722\*11.624\*6.572  $\mu\text{m}$ , Dark gray: Ni, Light gray: YSZ).

that FIB milling was precisely controlled to keep the milling direction being perpendicular to the observation surface throughout the “cut and see” sequence in this study resulting no noticeable image inclination. Therefore the image alignment was done only by parallel shifting in  $x$ - and  $y$ -directions.

Separation of three phases is next performed for each SEM image. A glance at Fig. 2 (b) reveals that the pore region filled with epoxy resin is easily distinguished as it appears as thick black region. On the other hand, the separation of solid part into the Ni phase and the YSZ phase needs careful treatment. EDX analysis is performed at the beginning or the end of FIB-SEM observation to correlate brightness with two solid phases. Obtained correlation is applied to all images of the same data series. The separation of three phases is performed semi-automatically with some manual corrections to finalize the process.

The data set after the alignment and the phase separation processes is ready for the 3-D structure reconstruction. Figure 3 shows an example of Ni-YSZ anode microstructure reconstructed in this study.

### **Quantification of geometric parameters**

Geometric parameters of the sample anode are evaluated using the 3-D structure data. TPB density and tortuosity factors are important geometric parameters not only to quantitatively understand anode performance but to develop reliable models for numerical simulations. It seems, however, there is no established method to evaluate them from FIB-SEM dataset even though the accuracy of the estimation depends on the evaluation procedures. In this study, we apply two different evaluation procedures to each parameter and compare their results to ensure reliability of the estimation.

**TABLE II.** Volume fractions of three phases. [%]

	Pore	Ni	YSZ
Sample 1	47.5	27.4	25.1
Sample 2	49.6	25.3	25.1
Sample 3	49.5	24.5	26.0

### Volume fractions

3-D reconstruction process was performed for three sample data sets and supplied for the quantification study. As one of the most fundamental properties, Table 2 summarizes volume fractions of each phase for three samples. Because the sample anode is fabricated to be Ni:YSZ=50:50 vol%, the ratio of Ni and YSZ volume fractions is expected to be unity. It is actually calculated as 1.09, 1.01 and 0.94, respectively. We judged this variation is not negligible but still within the acceptable range. The fact that even a fundamental property like volume fraction suffers such variation implies that a larger sample size is preferred for the quantitative analysis. Increasing sample size, however, inevitably lowers spatial resolution. The balance between the sample size and the spatial resolution is an essential problem of this method and is strongly related to the fabrication process of cells. In the latter sections we take Sample 2 as a representative sample. It was re-sampled to have 62nm\*62nm\*62nm cubic voxel structures because some of the following analyzing methods require such voxel structure. Resulting sample size was 18.600 $\mu\text{m}$ \*8.432 $\mu\text{m}$ \*6.200 $\mu\text{m}$ .

### Three phase boundary density

Volume expansion method. TPB forms lines in the 3-D reconstructed field. Suppose we slightly expand each phase outward in the virtual field, the overlapped regions form tube-like volumes which contain the TPB lines inside. In this method the centerlines of those tubes are taken as lines that represent TPBs and their lengths are measured. It is worth noting that lines obtained through this method theoretically match TPBs if the spatial resolution of 3-D reconstruction is high enough and the volume expansion is limited to be infinitely small. The effect of spatial resolution is roughly examined by applying it to a well defined problem. It is confirmed that this method provides reasonable results for structures having characteristic length over 10 voxels. TPB density estimated by the volume expansion method is 2.487  $\mu\text{m}/\mu\text{m}^3$  for the sample of this study.

Centroid method. The phase of each voxel is assigned as either Ni, YSZ or pore. If neighboring four voxels are composed of every three phases, and also if the phases of the diagonal voxels are not the same, the line segment surrounded by the four voxels are defined as three phase boundary. Then, triangles are defined by the neighboring three midpoints of the three phase boundary segments. The three phase boundary length is calculated as the distance between the centroids of these triangles. Table 3 shows the calculated three phase boundary length. Total TPB length as well as the active TPB lengths in  $x$ ,  $y$  and  $z$  directions are listed in the table.

**TABLE III.** Three phase boundary length by centroid method.

	TPB length ( $\mu\text{m}/\mu\text{m}^3$ )
Total	2.556
Active TPB ( $x=0 \mu\text{m}$ : Electrolyte, $x=18.6 \mu\text{m}$ : Current Collector)	1.539
Active TPB ( $x=0 \mu\text{m}$ : Current Collector, $x=18.6 \mu\text{m}$ : Electrolyte)	1.730
Active TPB ( $y=0 \mu\text{m}$ : Electrolyte, $y=8.43 \mu\text{m}$ : Current Collector)	1.598
Active TPB ( $y=0 \mu\text{m}$ : Current Collector, $y=8.43 \mu\text{m}$ : Electrolyte)	1.854
Active TPB ( $z=0 \mu\text{m}$ : Electrolyte, $z=6.2 \mu\text{m}$ : Current Collector)	1.719
Active TPB ( $z=0 \mu\text{m}$ : Current Collector, $z=6.2 \mu\text{m}$ : Electrolyte)	1.919

### Tortuosity factor

LBM based calculation. Assuming that Ni and YSZ are perfect electronic and ionic conductors, gaseous, electronic and ionic diffusion equations are solved inside each of the obtained three dimensional structures of Ni, YSZ and pore phases:

$$\frac{\partial}{\partial x_\alpha} \left( D \frac{\partial C}{\partial x_\alpha} \right) = 0 \quad [1]$$

$$\frac{\partial}{\partial x_\alpha} \left( \frac{\sigma_{el}}{F} \frac{\partial \eta_{e^-}}{\partial x_\alpha} \right) = 0 \quad [2]$$

$$\frac{\partial}{\partial x_\alpha} \left( \frac{\sigma_{io}}{2F} \frac{\partial \eta_{O^{2-}}}{\partial x_\alpha} \right) = 0 \quad [3]$$

where  $x_\alpha$  represents  $x, y, z$  directions,  $C$  is concentration,  $D$  is diffusion coefficient,  $\eta$  is electrochemical potential,  $\sigma$  is conductivity and  $F$  is Faraday's constant. The Lattice Boltzmann Method (LBM) (18) is used to solve Eqs. [1] to [3]. The LB equation with the LBGK model in the collision term is written as follows:

$$f_i(\mathbf{x} + \mathbf{c}_i \Delta t, t + \Delta t) = f_i(\mathbf{x}, t) - \frac{1}{t^*} [f_i(\mathbf{x}, t) - f_i^{eq}(\mathbf{x}, t)] + w_i \Delta t \quad [4]$$

In Eq. [4],  $f_i$  represents the velocity distribution function with velocity  $\mathbf{c}_i$  in the  $i$ -th direction, and  $f_i^{eq}$  is the Maxwellian local equilibrium distribution. For the 3D LBM simulation, D3Q15 ( $i = 1-15$ ) or D3Q19 ( $i = 1-19$ ) models are commonly used. However, it has been shown that, in case of simple diffusion simulation, D3Q6 ( $i = 1-6$ ) model can be used with a slight loss of accuracy (19). So the D3Q6 model is used in this work. The relaxation time is  $t^*=0.99$  and fixed for all simulations. Dirichlet boundary conditions are applied at the boundary surfaces. From LBM calculation, effective diffusion coefficient  $D^{eff}$  of the gas phase, effective conductivities of the Ni and YSZ phases,  $\sigma_{Ni}^{eff}$  and  $\sigma_{YSZ}^{eff}$ , can be obtained. Since Eqs. [1] to [3] are similar, tortuosity factors for each phase,  $\tau_{pore}$ ,  $\tau_{Ni}$  and  $\tau_{YSZ}$ , are defined as follows:

$$D^{eff} = \frac{V_{Pore}}{\tau_{Pore}} D \quad [5]$$

$$\sigma_{eli}^{eff} = \frac{V_{Ni}}{\tau_{Ni}} \sigma_{el} \quad [6]$$

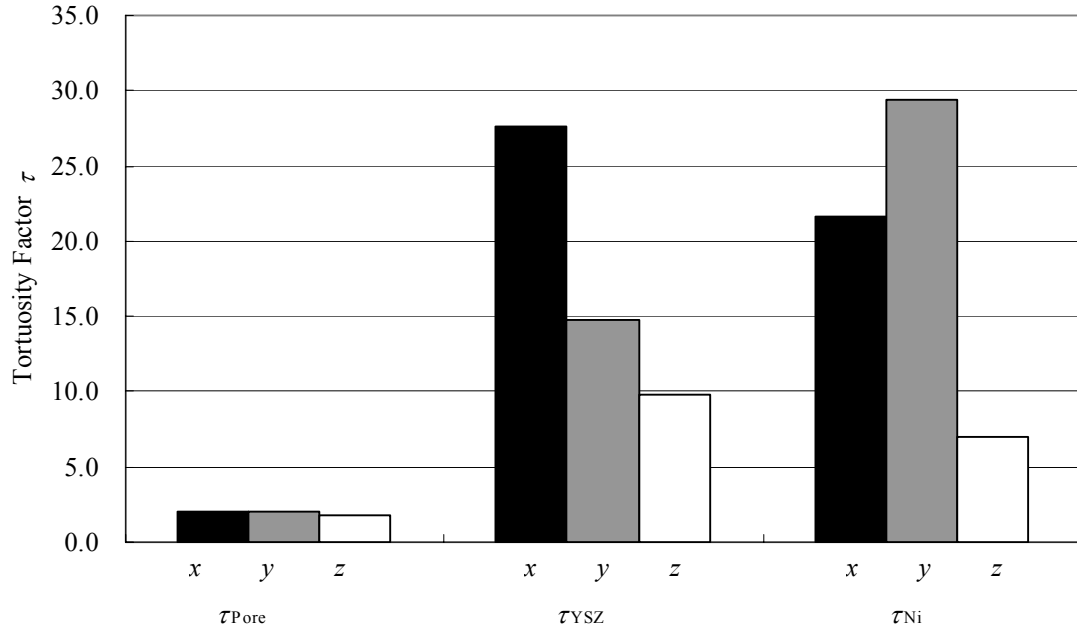


Figure 4. Predicted tortuosity factors  $\tau_{\text{pore}}$ ,  $\tau_{\text{Ni}}$  and  $\tau_{\text{YSZ}}$  by LBM

$$\sigma_{io}^{\text{eff}} = \frac{V_{\text{YSZ}}}{\tau_{\text{YSZ}}} \sigma_{io} \quad [7]$$

where  $V_{\text{Pore}}$ ,  $V_{\text{Ni}}$  and  $V_{\text{YSZ}}$  are the volume fractions of Pore, Ni and YSZ phases, respectively. Note that tortuosity factor is different from tortuosity which is defined as the ratio of the average winded pore length to the thickness of the porous material (20). Tortuosity factor is much more important since it is directly related to effective diffusivity or conductivity. As Eqs. [1] to [3] are solved in three directions, tortuosity factors have three different values corresponding to  $x$ ,  $y$  and  $z$  directions. Figure 4 shows the calculated tortuosity factors. Cross sectional areas normal to  $x$ ,  $y$  and  $z$  directions are  $52.3 \mu\text{m}^2$ ,  $115.3 \mu\text{m}^2$  and  $156.8 \mu\text{m}^2$ , respectively. As can be seen from the figure, tortuosity factors of solid phases,  $\tau_{\text{Ni}}$  and  $\tau_{\text{YSZ}}$ , show very large values for  $x$  and  $y$  directions. On the other hand,  $\tau_{\text{pore}}$  shows nearly the same values for three directions. It is considered that winded electronic and ionic paths are disconnected at the side boundaries for  $x$  and  $y$  directions. From Fig. 4, it is evident that the processed volume size is not large enough for evaluating effective conductivities of the solid phases for the present sample.

Random walk approach. Tortuosity factor is one of the most important factors related with mass transport in the porous structure. It can be statistically calculated from random walk process of non-sorbing particles. As the first step of this method, a number of random walkers are randomly distributed to the pore voxels. Each walker randomly chooses one of the neighboring voxels as a possible location of itself in the next time step. If the selected neighboring voxel represents pore part, the walker migrates to that voxel. If the selected voxel is a solid voxel, the walker stays at the current voxel and waits for

next time step. In this procedure neither absorption nor desorption is taken into account. While repeating this procedure, the mean square displacement of random walkers is calculated as follows:

$$\langle r^2(t) \rangle = \frac{1}{n} \sum_{i=1}^n [\{x_i(t) - x_i(0)\}^2 + \{y_i(t) - y_i(0)\}^2 + \{z_i(t) - z_i(0)\}^2] \quad [8]$$

where  $n$  is the total number of random walkers, and  $\langle \rangle$  means an ensemble average. Since the mean square displacement  $\langle r^2 \rangle$  is proportional to time, the diffusion coefficient,  $\mathcal{D}$ , of non-sorbing species is related to the time-derivative of  $\langle r^2 \rangle$  (21, 22).

$$\langle r^2(t) \rangle = 6\mathcal{D}t \quad \Rightarrow \quad \mathcal{D} = \frac{1}{6} \frac{d\langle r^2(t) \rangle}{dt} \quad [9]$$

The mean square displacement in a porous media,  $\langle r^2 \rangle_{\text{pore}}$ , takes lower value than that obtained in a free space,  $\langle r^2 \rangle_{\text{free}}$ , because of the obstruction effects of solids. The degree of reduction is measured quantitatively by the tortuosity factor defined as follows:

$$\tau = \frac{\mathcal{D}_{\text{free}}}{\mathcal{D}_{\text{pore}}} \quad [10]$$

When the porous media has an anisotropic pore structure, the mean square displacement  $\langle r^2 \rangle$  may be divided into directional mean square displacements,  $\langle x^2 \rangle$ ,  $\langle y^2 \rangle$ , and  $\langle z^2 \rangle$ .

$$\langle x^2(t) \rangle = \frac{1}{n} \sum_{i=1}^n \{x_i(t) - x_i(0)\}^2 \quad [11]$$

$$\langle y^2(t) \rangle = \frac{1}{n} \sum_{i=1}^n \{y_i(t) - y_i(0)\}^2 \quad [12]$$

$$\langle z^2(t) \rangle = \frac{1}{n} \sum_{i=1}^n \{z_i(t) - z_i(0)\}^2 \quad [13]$$

Then anisotropic tortuosity factors are calculated with similar relations as Eqs. [9] and [10].

To execute random walk process, a large scale random number is needed. We use ‘‘SIMD-oriented Fast Mersenne Twister (SFMT)’’ as a high performance pseudo-random number generator.

Prior to the calculation, the pores connected to the computational domain surface boundaries are extracted from stacked images as ‘‘effective pores’’ and isolated pores are excluded from the calculation. This is because the isolated pores do not contribute to the gas diffusion and may cause an overestimation of the tortuosity factor. In order to obtain an accurate value of the tortuosity factor, long time step and a large number walker are necessary. However, as the time step proceeds, random walkers may go out of the stacked images. A mirror symmetric boundary condition is applied to solve this problem,

as it guarantees the connectivity of pore structure across the boundaries. The calculation is carried out for 100,000 time steps with 1,000,000 random walkers. Data obtained during the first 10,000 steps are omitted in the calculation of the diffusion coefficient because walkers have not yet experienced the porous solid structure at the early stage of random walk. It is worth noting that this was only 3 hours calculation on a standard desktop PC. Random walk-based calculations require less computational time and cost. Table 4 summarizes the tortuosity factors estimated by random walk method. This result agrees very well with the LBM-based tortuosity factor calculation with less than 1% difference.

**TABLE IV.** Anisotropic tortuosity factors of pore region calculated by two methods.

	$\tau_x$	$\tau_y$	$\tau_z$
LBM	2.031	2.056	1.834
Random walk	2.028	2.054	1.818

### Conclusion

Three dimensional microstructure of a Ni-8YSZ anode is quantified by means of dual beam FIB-SEM. In-lens secondary electron detector was used, which provided clear contrast between Ni and YSZ phases with submicron resolution. From the reconstructed three dimensional structure, microstructural parameters such as volume fraction, TPB length and tortuosity factors are quantified. TPB density is estimated by the volume expansion method and the centroid method proposed in this study and their results match each other with less than 3 % difference. Tortuosity factors are evaluated by the LBM based calculation and by the random walk approach. Tortuosity factors of pore region evaluated by both methods match well each other with less than 1 % difference. It proves the reliability of analyzing methods proposed in this study. It is also revealed that the volume size of the sample used in this study is not large enough for the quantification of effective conductivities of Ni and YSZ.

### Acknowledgments

This work was supported by the New Energy and Industrial Technology Development Organization (NEDO) under the Development of System and Elemental Technology on Solid Oxide Fuel Cell (SOFC) Project.

### References

1. S. C. Singhal and K. Kendall, High Temperature Solid Oxide Fuel Cells, Elsevier (2002).
2. M. Mogensen and S., Skaarup, *Solid State Ionics*, **86-88**, 1151-1160 (1996) .
3. N. Q. Minh, *J. Am. Ceram. Soc.* 76, 563-588 (1993).
4. H. Koide, Y. Someya, T. Yoshida and T. Maruyama, *Solid State Ionics*, **132**, 253-260 (2000).
5. A. Atkinson, S. Barnett, R. J. Gorte, J. T. S. Irvine, A. J. Mcevoy, M. Mogensen, S. C. Singhal and J. Hohns, *Nature Materials*, **3**, 17-27 (2004).
6. H. Abe, K. Murata, T. Fukui, W.-J. Moon, K. Kaneko and M. Naito, *Thin Solid Films*, **496**, 49-52 (2006).

7. T. Fukui, K. Murata, S. Ohara, H. Abe, M. Naito and K. Nogi, *J. Power Sources*, **125**, 17-21, (2004).
8. H. Itoh, T. Yamamoto, M. Mori, T. Horita, N. Sakai, H. Yokokawa and M. Dokiya, *J. Electrochem. Soc.*, **144**(2), 641-646 (1997).
9. W. Z. Zhu and S. C. Deevi, *Materials Sci. Eng.*, **A362**, 228-239 (2003).
10. Y.-J. Leng, S.-H. Chan, K.-A. Khor, S.-P. Jiang and P. Cheang, *J. Power Sources*, **117**, 26-34 (2003).
11. S.-D. Kim, H. Moon, S.-H. Hyun, J. Moon, J. Kim and H.-W. Lee, *Solid State Ionics*, **177**, 931-938 (2006).
12. J.-H. Yu, G.-W. Park, S. Lee and S.-K. Woo, *J. Power Sources*, **163**, 926-932 (2007).
13. J. R. Wilson, W. Kobsiriphat, R. Mendoza, H.-Y. Chen, J.M. Hiller, D. J. Miller, K. Thornton, P.W. Voorhees, S. B. Adler and S. Barnett, *Nature Materials*, **5**, 541-544 (2006).
14. D. Gostovic, J. R. Smith, D. P. Kundinger, K. S. Jones and E. D. Wachsman, *Electrochemical and Solid-State Letters*, **10** (12), B214-B217 (2007).
15. J. R. Smith, A. Chen, D. Gostovic, D. Hickey, D. P. Kundinger, K. L. Duncan, R. T. DeHoff, K. S. Jones and E. D. Wachsman, *Solid State Ionics*, **180**, 90-98 (2009).
16. J. R. Wilson, M. Gameiro, K. Mischaikow, W. Kalies, P. Voorhees and S. Barnett, *Microsc. Microanal.*, **15**, 71-77 (2009).
17. J. R. Izzo, Jr., A.S. Joshi, K. N. Grew, W. K. S. Chiu, A. Tkachuk, S. H. Wang and W. Yun, *J. Electrochem. Soc.*, **155** (5), B504-B508 (2008).
18. Y. Suzue, N. Shikazono and N. Kasagi, *J. Power Sources*, **184**, 52-59 (2008).
19. Th. Zeiser, P. Lammers, E. Klemm, Y. W. Li, J. Bernsdorf, G. Brenner, *Chem. Eng. Sci.*, **56**, 1697-1704 (2001).
20. N. Epstein, *Chem. Eng. Sci.*, **44**, 777-779 (1989).
21. Y. Watanabe, Y. Nakashima, *Computers & Geosciences*, **28**, 583-586, (2002).
22. Y. Nakashima, S. Kamiya, *Journal of Nuclear Science and Technology*, **44**, 1233-1247, (2007).